AFRL-AFOSR-VA-TR-2018-0338

Single-site imaging of fermions in two-dimensional optical lattices

Joseph Thywissen
UNIVERSITY OF TORONTO

05/09/2018
Final Report

Air Force Research Laboratory
AF Office Of Scientific Research (AFOSR)/ RTB1
Arlington, Virginia 22203
Air Force Materiel Command

REPORT DOCUMENTATION PAGE

Form Approved
OMB No. 0704-0188

1. REPORT DATE *(DD-MM-YYYY)*	2. REPORT TYPE	3. DATES COVERED *(From - To)*
13-09-2018	Final Performance	01 Feb 2013 to 31 Jan 2018

4. TITLE AND SUBTITLE
Single-site imaging of fermions in two-dimensional optical lattices

5a. CONTRACT NUMBER

5b. GRANT NUMBER
FA9550-13-1-0063

5c. PROGRAM ELEMENT NUMBER
61102F

6. AUTHOR(S)
Joseph Thywissen

5d. PROJECT NUMBER

5e. TASK NUMBER

5f. WORK UNIT NUMBER

7. PERFORMING ORGANIZATION NAME(S) AND ADDRESS(ES)
UNIVERSITY OF TORONTO
27 KINGS COLEGE CIR
TORONTO, 21421016 CA

8. PERFORMING ORGANIZATION REPORT NUMBER

9. SPONSORING/MONITORING AGENCY NAME(S) AND ADDRESS(ES)
AF Office of Scientific Research
875 N. Randolph St. Room 3112
Arlington, VA 22203

10. SPONSOR/MONITOR'S ACRONYM(S)
AFRL/AFOSR RTB1

11. SPONSOR/MONITOR'S REPORT NUMBER(S)
AFRL-AFOSR-VA-TR-2018-0338

12. DISTRIBUTION/AVAILABILITY STATEMENT
A DISTRIBUTION UNLIMITED: PB Public Release

13. SUPPLEMENTARY NOTES

14. ABSTRACT
We report on the results obtained across the five-year AFOSR-supported project, whose goals were to develop a system capable of imaging ultracold lattice fermions with single-atom sensitivity; and using this tool to perform a quantum simulation that improves our understanding of materials. Both of these objectives were achieved. We built an ultrahigh vacuum system with exceptional optical access, and used it to image individual fermionic potassium atoms in a 527-nm-period optical lattice. Atoms remain at individual sites of a 0.3-mK-deep lattice, with a pinning lifetime of 70 seconds, while scattering thousands of photons per second. Comparison of multiple images reveals a single-atom fidelity of 94%. These techniques are refined by combining Raman sideband cooling with electromagnetically induced transparency (EIT). We then study the transport properties of fermions in a cubic lattice through micron -scale response dynamics to an alternating external force. Our technique measures both on- and off-diagonal conductivity in one spatial plane, which provides a model-free measurement of the Hall effect. Sum rules are used to relate the observed conductivity to thermodynamic properties such as kinetic energy, and to test the validity of single-band models. We explore the effect of lattice depth, temperature, interaction strength, and atom number on conductivity. Using a relaxation-time approximation, we extract the transport time of current, and show that

15. SUBJECT TERMS
fermions

16. SECURITY CLASSIFICATION OF:			17. LIMITATION OF ABSTRACT	18. NUMBER OF	19a. NAME OF RESPONSIBLE PERSON
a. REPORT	b. ABSTRACT	c. THIS PAGE			CURCIC, TATJANA

Unclassified	Unclassified	Unclassified	UU	**PAGES**	**19b. TELEPHONE NUMBER** *(Include area code)* 703-696-6204

Final Performance Report

Dates: 1 Feb 2013 to 31 Jan 2018
Contract: FA9550-13-1-0063
Institution: University of Toronto
PI: J. H. Thywissen

This document reports the technical and scientific progress achieved during the contract FA9550-13-1-0063, "Single-site imaging of fermions in a two-dimensional optical lattice," funded by the Air Force Office of Sponsored Research over the period 1 Feb 2013 to 31 Jan 2018.

The purpose of this research program is to investigate ultracold fermions in periodic potentials. In particular, we have pioneered the development of a new tool that allows in-situ studies of conductivity in ultracold systems. The steps towards this achievement are summarized in the Results section of this report.

CONTENTS

I. EXPERIMENTAL INFRASTRUCTURE

In the previous AFOSR funding cycle (2010–2013), we built a system compatible with high numerical-aperture light collection from atoms in a three-dimensional optical lattice. This system is illustrated in Figure 1. A typical experimental cycle proceeds as follows: (a) Atoms are collected from vapor in a magneto-optical trap (MOT). Two isotopes are used: fermionic potassium 40 (^{40}K) and bosonic rubidium 87 (^{87}Rb). Trapped atoms are laser cooled, and transferred to a 3D quadrupole trap in this cell. (b) Atoms are transported magnetically from the MOT chamber to the lattice chamber. The motivation for this transfer is to improve the vacuum environment (by more than 10^4) and increase optical access. (c) In the lattice chamber, atoms are evaporatively cooled. This occurs in three stages: first, in a bare quadrupole trap in the middle of the chamber; second, when moved closer to the microscopy window, in a plugged quadrupole trap; and third, after transfer to the crossed optical dipole trap (XDT). (d) Atoms are loaded into the optical lattice, and an experiment is performed. The lattice beams are held at a low power for these experiments, so that the tunnelling rate is sufficiently high. A typical lattice depth is less than $10\,E_R$, where E_R is a recoil energy, the maximum bandwidth of the lowest Bloch band. (e) Finally, atoms are imaged by in-situ fluorescence. For this imaging phase, the lattice depth is increased to over $10^3\,E_R$.

II. RESULTS

A. Single-atom imaging of fermionic potassium in an optical lattice

The technical advance at the core of the proposed work was to realize in-situ imaging of fermions in an optical lattice, with single-atom sensitivity. At the time of the proposal, this was an outstanding challenge for the field of ultracold atoms, and had not been realized in any laboratory. We successfully realized this goal in 2015 [1], as did four other groups [2–5]. Our approach is distinguished by a unique imaging configuration, and takes a further step by

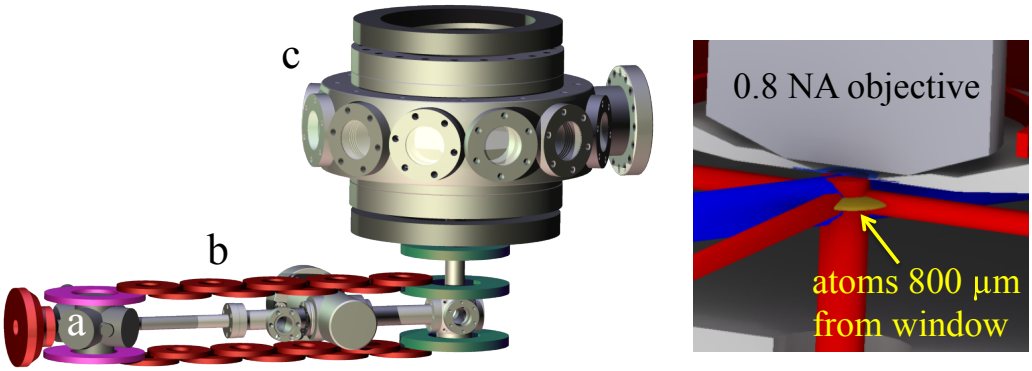

FIG. 1. Vacuum system enabling extreme optical access to cold atoms. Atomic sources produce a vapor in a glass MOT (magneto-optical trap) chamber (labeled **a**), which is laser cooled and trapped. A magnetic transport system (labeled **b**) moves the atoms a total path length of 0.5 m to the lattice chamber (labeled **c**). The latter has fourteen windows allowing optical access along seven lines: these are used for microscopy, the optical lattice, the optical dipole traps, imaging light, laser cooling light, and beams to sculpt the trapping environment.

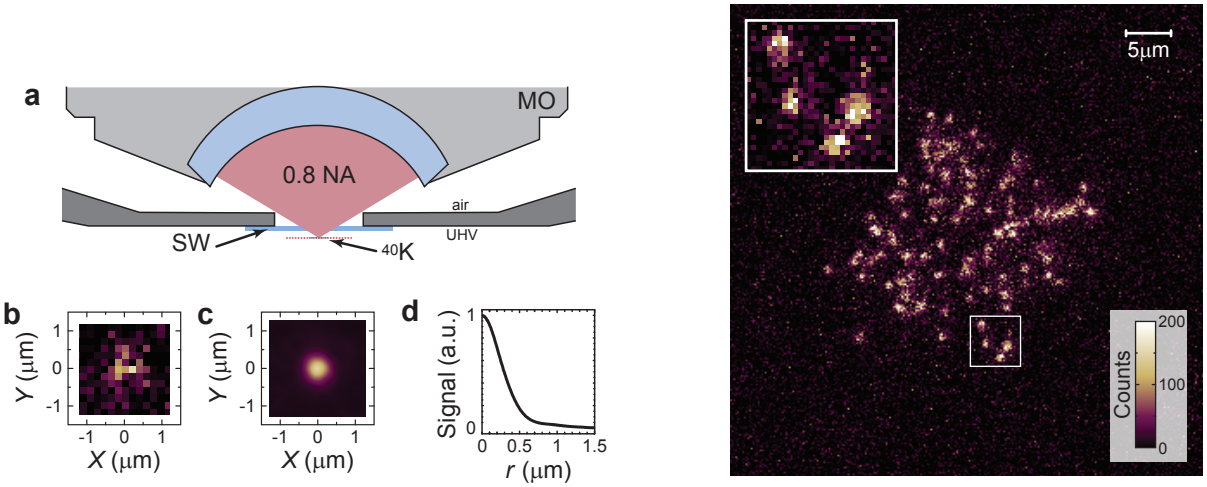

FIG. 2. **Microscopy.** (**a**) A sapphire window (SW) with a thickness of 200 μm and a clear aperture of 5 mm separates UHV from air. This allows for the placement of a microscope objective (MO) with NA = 0.8 and 3 mm working distance outside the vacuum with its focal plane on the inside. (**b**) Single-shot image of a single atom. With image magnification of 78×, each camera pixel has a virtual size of 192 nm. (**c**) Averaging the signal from 200 isolated atoms in the imaging plane yields the effective PSF of the imaging system. The coordinates X and Y are aligned with the principal axes of the images. (**d**) The radial average of the PSF has a FWHM of 0.60(1) μm. Note that this effective PSF includes not only optical effects but also the finite size of lattice orbitals and drifts of the lattice during exposure. **Right:** High-resolution fluorescence image of fermionic potassium atoms in a single sparsely filled plane of a 527-nm-period cubic optical lattice. The false-color scale indicates the number of counts recorded by an electron-multiplying CCD camera, where one photoelectron corresponds to 16 counts. Atoms outside of a 40×40 site box have been removed using the addressing protocol described in the main text. In the inset, one can clearly discern individual atoms. In this 2.6-s-long exposure, an average of ∼160 photons are detected per atom. Since 2015, further improvements increased the brightness of such images five-fold.

implementing three-dimensional spatial addressing. Figure 2 illustrates these abilities with a high-resolution image of ^{40}K atoms sparsely filling a selected 40-site × 40-site × 1-site volume.

At the heart of our apparatus is a microscope objective with a numerical aperture (NA) of 0.8, placed outside of an ultra-high vacuum (UHV) chamber, 2.0 mm above a 200-μm-thick sapphire window [see Fig. 2(a)]. The focal plane of the imaging system is located inside the vacuum, 0.8 mm beyond the thin window. Sapphire is sufficiently hard that this thin substrate can sustain atmospheric pressure with a clear aperture of 5 mm. At the same time, it contributes less spherical aberration than a standard millimeter-thick viewport, since spherical aberration scales as the cube of

thickness. The effective point spread function (PSF) of the full imaging system is shown in Figs. 2(c,d) as the average over images of 200 isolated single atoms, centered to sub-pixel precision. Its full width at half maximum (FWHM) of $0.60(1)\,\mu$m is larger than the diffraction limit of $0.5\,\mu$m, yet small enough to reconstruct the lattice occupation.

Site-resolved reconstruction of single atoms requires that each atom remains pinned in the lattice while scattering photons. Although direct fluorescence imaging with short light pulses has been demonstrated for Yb [6], it is not viable for sub-micron single-atom microscopy of alkali atoms. Instead, light scattering must be accompanied with laser cooling. Since red-detuned D_2 molasses [7–9] is compromised in ^{40}K due to the inverted hyperfine structure of the $4P_{3/2}$ excited state, we explored in-situ cooling on the $4S_{1/2} \rightarrow 4P_{1/2}$ (D_1) transition at 770.1 nm in ^{40}K. Unlike for D_1 cooling in free space [10–12] or in weak traps [13, 14] where a Sisyphus mechanism creates a gray molasses [15], we observe that a polarization gradient is not essential for cooling in a deep lattice. Instead, dark-state coherence establishes an EIT window that suppresses carrier scattering, while creating an absorption resonance at the red trap sideband, thereby cooling the tightly bound atoms [2, 16]. Multicolor Raman sideband cooling realizes a similar mechanism [17–19], and has also been used for the site-resolved imaging of fermionic atoms [3–5].

In our 2015 work, we used EIT cooling. Two "coupling" beams (C_{xy} and C_z) are near the $4S_{1/2}(F = 9/2) \rightarrow 4P_{1/2}(F' = 7/2)$ transition, while a weaker "probe" beam (P_{xy}) is near the $4S_{1/2}(F = 7/2) \rightarrow 4P_{1/2}(F' = 7/2)$ transition with differential detuning of δ from the Raman resonance across ground states. The common-mode detuning Δ from the $F' = 7/2$ state of all beams depends on the depth of the optical lattice due to the Stark shift, with larger lattice depth corresponding to smaller Δ. For atoms in the center of the lattice at the depth used for imaging, the Stark shift of the D_1 transition is measured to be $2\pi \times 68$ MHz, and our cooling beams are detuned by $\Delta = 2\pi \times 36$ MHz. The vertical cooling beam ("C_z") beam has a power of $2\,\mu$W, P_{xy} has $2\,\mu$W and is retroreflected; the horizontal cooling beams (C_{xy}) has $40\,\mu$W, providing Rabi frequencies of $2\pi \times 2.3$ MHz, $2\pi \times 1.3$ MHz, and $2\pi \times 4.2$ MHz respectively. Applying these beams scatters photons from the trapped atoms, while the EIT cooling mechanism prevents the atoms from heating out of the lattice sites. Time-of-flight expansion from a 3D lattice after band mapping shows that the majority of atoms remain in the ground vibrational band during imaging.

Images such as Fig. **??** reveal the binary filling of all lattice sites in the selected region, with the help of additional information about the lattice periodicity and the PSF. From a number of similar images, we determine the orientation and apparent period of the optical lattice through evaluation of the relative positions of more than 2000 isolated atoms. Comparing to the known lattice spacing of $\lambda_L/2$ yields the magnification of our imaging system (78×). With the lattice angles and magnification determined, we can reconstruct the lattice occupation $\in \{0, 1\}$ from each fluorescence image. We expect the apparent lattice occupation to be parity sensitive due to light-assisted collisions [8, 9], however, our average filling is $\ll 1$ atom per site so that occupancies larger than one are rare. Figures 3(a-d) illustrates the steps taken by our reconstruction algorithm to digitize a raw fluorescence image via sharpening and site-binning. Histograms of single-site signals are shown in Figs. 3(e,f).

The fidelity of imaging and reconstruction is assessed by comparing digitized images from two sequential exposures of the same arrangement of atoms. Exposures are separated by the 0.4 s required for camera read-out, during which atoms are still laser-cooled. By counting the number of atoms in the second digitization that either appear at an empty site or disappear from an occupied one, we calculate the fraction of atoms which are pinned, hop to a different site, or are lost completely in the second exposure. Figure 4 shows these measures versus several critical imaging parameters.

Figure 4(a) shows that optimal cooling is observed for $\delta = 0$ kHz, as was found in prior work [2, 16]. Here, the dressed ground state is maximally dark to elastic scattering, and inelastic scattering is biased towards red (cooling) transitions. Figure 4(b) shows that long exposures are possible with high fidelity. At short (< 2 s) exposure times, the apparent hopping fraction is high, due to errors in reconstruction with insufficient signal. However at longer exposure times, reconstruction errors are negligible, and loss and hopping approach constant rates of $0.4(3)\%\text{s}^{-1}$ and $1.1(2)\%\text{s}^{-1}$, respectively. This loss rate is consistent with a $1/e$ trap lifetime of >200 s, and a pinned fraction lifetime of 67(9) s.

Figures 4(c,d) evaluate the conditions under which a modulated C_z provides sufficient cooling to the vertical degree of freedom to maintain fidelity. Reducing the chopping frequency below 100 Hz results in a decrease in the fraction of atoms that are pinned to their sites. Fig. 4(d) shows that the rate of loss and hopping increases if the duty cycle of C_z is lower than 30%, at a chopping rate of 100 Hz. Thus, a high pinned atom fraction is observed with $\gtrsim 3$ ms cooling pulses. Combined with the inferred scattering rate, this suggests that approximately six photons can be scattered between vertical cooling cycles.

In optimal conditions, we find that 94(2)% of atoms stay pinned to the same lattice site in a sequence of two images. This is comparable to performance reported in Refs. 2–5, where pinning fidelity between successive images ranged from 92% to 95%. The fraction of atoms lost in the second image can be as low as 2(1)%. The rest of the 6(2)% of atoms that do not stay pinned either hop or are incorrectly reconstructed in the first or second frame. The optimal exposure time must compromise between signal and hopping during imaging, as shown in Fig. 4(b). This optimum will also depend on lattice filling fraction, since true hopping will become more problematic at high density, where

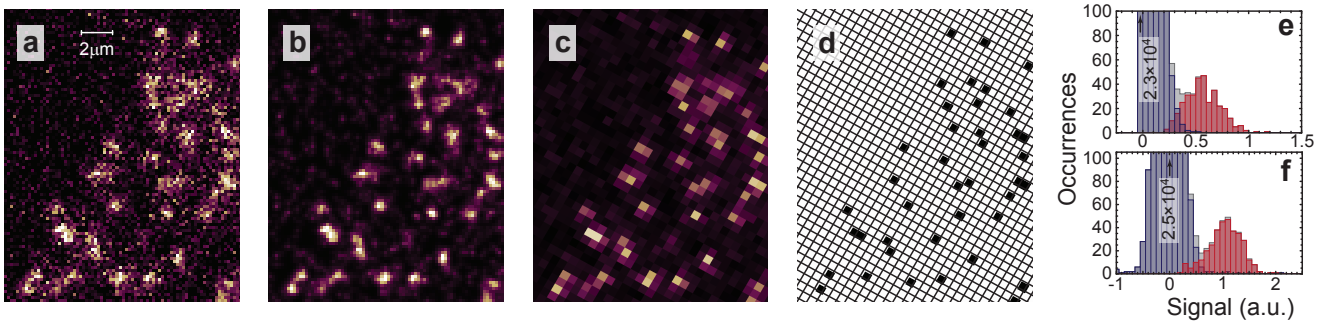

FIG. 3. (Color online) Reconstruction of the lattice occupation. (a) Magnified subimage of Fig. **??**. (b) Deconvolution of the image with the PSF [see Fig. 2(c)] gives a sharpened image which we use to pin the lattice grid. (c) A lattice-site binned image is then used to select potentially occupied sites via a threshold. (d) The final best-fit digitization is determined by comparing all possible occupation patterns for the selected sites and their immediate neighbors with the sharpened image. In this step we allow for discrete variation of brightness of ±20%, and we assume a Gaussian spatial distribution for each atom with a width determined by the typical feature size in the sharpened image. (e) Histogram of signal per lattice site obtained from twelve sharpened and binned images similar to (c). Gray bars correspond to the signal from all lattice sites, while the red and blue bars, respectively, display the signal from sites determined to be occupied or unoccupied. (f) Histogram of signal obtained from fits of Gaussian functions to the same images used for (e). Here, the signal for each site is obtained from a simultaneous fit to the sharpened subimage of the target site and its immediate neighbors. The width of the Gaussian functions is the same as for the digitization step.

such events will more likely eject a pair of atoms due to light-assisted collisions [7–9].

B. Measuring conductivity of ultracold atoms in an optical lattice

Measuring conductivity has proven to be a powerful discovery tool for new physics in materials. However, a first-principles connection between macroscopic functional properties and their microscopic quantum origins is challenging due to the non-equilibrium nature of transport, and the complex structure of many strongly correlated materials.

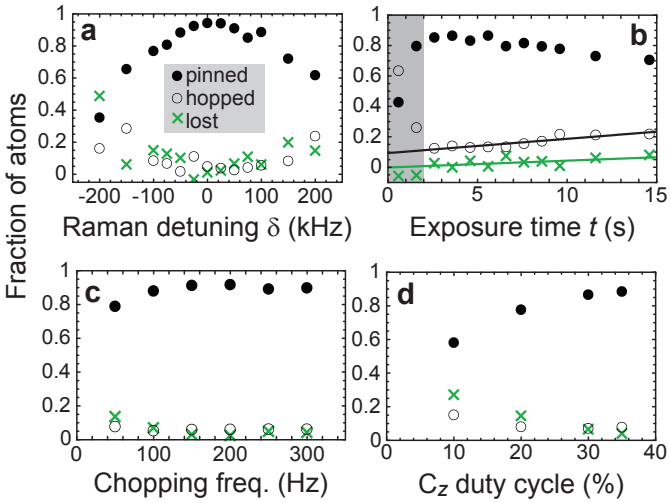

FIG. 4. Fidelity. Plots show the fraction of atoms in the first digitized image that are pinned (filled circles), hop to a different site (open circles), or are lost completely (crosses) in the successive image. Unless otherwise indicated, $\delta = 0$, the C_z chopping rate is 100 Hz, the C_z duty cycle is 35%, and the exposure time is 2.6 s with 0.4 s between exposures. Maximal pinning occurs for (a) Raman detuning $\delta \approx 0$; (b) exposure time between 2 s and 5 s; (c) a chopping frequency that is > 100 Hz; and (d) a duty cycle of C_z that is at least 30%. Lines shown in (b) are $0.002(28) + 0.004(3)\,t$ for loss fraction and $0.07(2) + 0.011(2)\,t$ for hopping fraction, and fit only to points at $t > 4$ s.

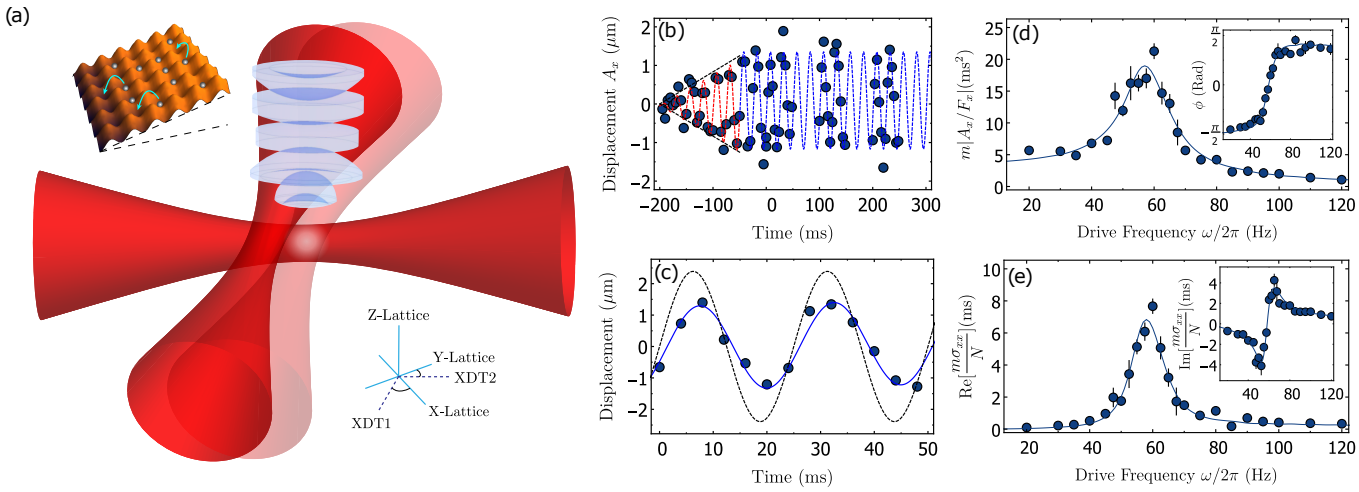

FIG. 5. **Measuring optical conductivity**. (a) A periodic force is applied by displacement in the xy plane of one or both of the crossed trapping beams. Atoms are imaged in situ with a high-resolution imaging system. (b) The displacement of the center of mass is measured after various drive times. The drive amplitude is increased linearly for the first 150 ms, and then held constant for 50 ms, before making a measurement. (c) The amplitude A and phase ϕ of the response (data points; with single-frequency fit shown as a blue line) relative to the applied force (black, dashed) are fit from c.m. oscillation across two periods. (d) Repeated measurements determine the frequency dependence of A and ϕ. (e) Real and imaginary conductivity are determined from (d) as described in the text.

Quantum simulations with ultracold atoms offer the prospect to bridge this gap, by comparing emergent phenomena in a simpler system to ab-initio calculations. The power of this approach lies in the ability to control initial conditions, observe dynamics, and tune elements of the underlying Hamiltonian.

In the final year of this project, we realized [20] the proposal of Wu, Taylor, and Zaremba [21], closely related to a proposal by Tokuno and Giamarchi [22], to measure the global conductivity of ultracold fermions in an optical lattice through center-of-mass (c.m.) dynamics. The sample is neutral; therefore, by conductivity we refer to the linear response parameter σ that is the ratio of particle-current J to an applied force F. Since the trap prevents a steady-state current response to a static force, the interesting response is the frequency-dependent $\sigma(\omega)$. We measure a quantity analogous to the optical conductivity of materials, typically studied through reflectivity and transmission of a sample [23]. However, since time scales are amplified by eight to ten orders of magnitude [24], typical features appear in the acoustic band instead of at microwave or optical frequencies.

The system studied is a balanced spin mixture of fermionic ^{40}K in a cubic optical lattice with period $a_L = 527\,\text{nm}$ and depth V. After sample preparation, typical conditions are as follows: $N \sim 10^4$ atoms in an equal mixture of the $m_F = -9/2$ and $m_F = -7/2$ spin states of the $F = 9/2$ ground-state manifold; lattice depth $s_L = 2.5$, where $s_L = V/E_R$ and $E_R = \hbar^2(\pi/a_L)^2/2m$; temperature $T \sim 1.5t_0$, where t_0 is the nearest-neighbor tunneling strength; and interaction strength $U \sim 0.7t_0$, from the background s-wave scattering length. These values are intentionally tuned, and the impact on system response studied throughout the experiment. Harmonic confinement is created by the three lattice beams and by two additional crossed dipole trap (XDT) beams [Fig. 5(a)]. Including all five beams, for typical $s_L = 2.5$, the trapping frequencies are $\omega_0 = 2\pi \times 65(3)\,\text{Hz}$ in the xy plane, and $\omega_z = 2\pi \times 220(10)\,\text{Hz}$ in the z direction.

Conductivity is measured as follows. After sample preparation, a periodic displacement of one or both of the XDT beams creates the analogue of the voltage in an electronic conductivity measurement. Drive frequencies range from 10 Hz to 200 Hz, with displacement amplitude typically a few μm. For XDT displacement $d_\beta(t)$ along directions $\beta = \{x, y\}$, the resultant force is $F_\beta = m\omega_{\text{XDT}}^2 d_\beta(t)$, where m is the bare mass and $m\omega_{\text{XDT}}^2$ is the spring constant of the XDT, with ω_{XDT} measured to be $2\pi \times 32(1)\,\text{Hz}$. The typical force ($\sim 10^{-26}\,\text{N}$) is what an elementary charge would experience in an electric field of $\sim 10^{-7}$ volts per meter. The amplitude of the periodic force is increased linearly over 150 ms, then held constant for 50 ms. This allows the system to come to a quasi-steady state [see Fig. 5(b)].

After a further variable delay time t of up to two drive periods, the dynamics are frozen by increasing the lattice depth to $60\,E_R$ in 0.1 ms. The in-situ density distribution of the cloud is recorded via fluorescence in our quantum gas microscope apparatus at $1000\,E_R$. Only the central four planes of the optical lattice are measured, to remain near the focal plane of the imaging system. Displacement in z is not measured, nor expected since forces are applied in the xy plane, and no Hall response is anticipated. The imaging process photo-associates atoms in doubly occupied

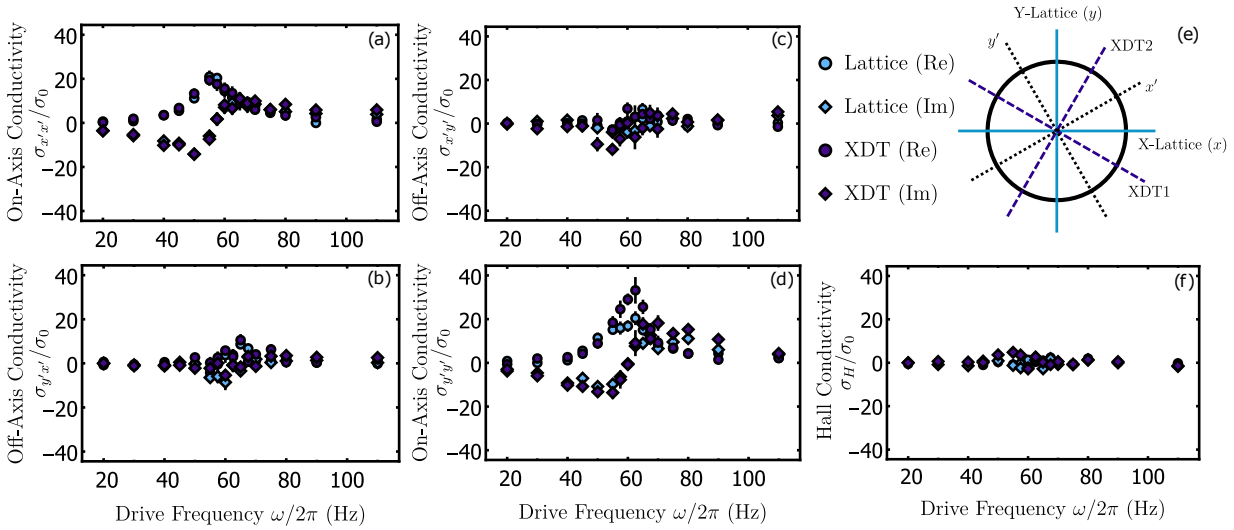

FIG. 6. **Tensor nature of conductivity.** The conductivity tensor is determined by measuring response when forcing along the lattice axes (x, y), and comparing to when forcing along the XDT axes, which differ by an angle of $\pi/6$. (a-d) The full conductivity tensor, reported in the basis (x', y'). On-diagonal terms shown in (a) and (d) are more prominent than off-diagonals in (b) and (c). (e) Axes used for forcing in the two sets of measurements are shown (blue, solid) and (purple, dashed). The tensors are expressed in a common (black, dotted) basis. (f) Hall conductivity σ_H/σ_0 is within experimental fluctuation of zero, as expected. All data shown here is for depth $s_L = 2.5$, $U/t_0 = 0.7$.

sites [8, 9]. In order to minimize this effect, we work in a low-filling regime, with typical $\langle n_\uparrow \rangle = \langle n_\downarrow \rangle = 0.12(1)$ per spin state, but average doublon fraction of only 0.02(1).

From in-situ fluorescence images, we measure a site-granulated c.m. position $\hat{R}_{\alpha=x,y} = \sum_{i,\sigma} r_{\alpha,i} \hat{n}_{i,\sigma}$, where $|i\rangle$ is the state describing an atom on lattice site i located at $r_{\alpha,i}$, that we fit to $R_\alpha(t) = A_\alpha \cos[\omega t - \phi_\alpha]$ [see Fig. 5(c,d)], where ω is the drive frequency, and not a fit parameter. We then deduce the steady-state bulk current from

$$\langle \hat{J}_\alpha(\omega) \rangle = N d \langle \hat{R}_\alpha(\omega) \rangle / dt \,, \tag{1}$$

where complex notation ($R_\alpha(\omega) = (A_\alpha/2) \exp[-i\omega t + i\phi_\alpha]$, etc.) is used in the frequency domain.

The global conductivity $\sigma_{\alpha\beta}$ can then be determined through Ohm's Law,

$$\langle \hat{J}_\alpha(\omega) \rangle = \sum_\beta \sigma_{\alpha\beta}(\omega) F_\beta(\omega), \tag{2}$$

so that in terms of fit variables and drive strength,

$$\sigma_{\alpha\beta} = \frac{N\omega A_\alpha}{iF_\beta} \exp[i\phi_\alpha]. \tag{3}$$

Figure 5(e) shows an example of the real and imaginary conductivity determined in this way for moderate lattice depth and weak interactions, $U/t_0 = 0.7$. Since we are measuring the optical conductivity of a harmonically trapped lattice system, the DC conductivity of the system is zero: the trap contributes a capacitive term to the impedance, which diverges at zero frequency. Instead, the real conductivity shows a resonance at the lattice-dressed trap frequency ω^*, here ≈ 60 Hz, with a full width smaller than 10 Hz. As required by the Kramers-Kronig relations, the imaginary conductivity follows a dispersive response at the same resonant frequency.

$\sigma_{\alpha\beta}$ is an extensive, complex tensor, with units of time over mass. Using the lattice spacing a_L as a natural length scale, we write the conductivity in dimensionless form: σ/σ_0 where $\sigma_0 \equiv a_L^2 N/\hbar$. The numerical value of σ_0 is $m\sigma_0/N \approx 175\,\mu$s, which is $\pi^2/2$ times the recoil time $\hbar/E_R$. σ_0 also gives the scale of the Mott-Ioffe-Regel limit.

Our experimental protocol allows us to provide a force to the sample along any axis. Choosing any two non-collinear axes enables the determination of the two-dimensional conductivity tensor $\sigma_{\alpha\beta}(\omega)$ describing transport in a plane. Knowledge of the tensor $\sigma_{\alpha\beta}(\omega)$ is of interest because it reveals spatial and temporal symmetries of the sample.

Figure 6(a-d) shows tensor conductivity determined through two different choices of pairs of forcing axes: either along the axes of the in-plane optical lattices, or along the axes of the XDT beams, which are rotated by $\pi/6$ from the

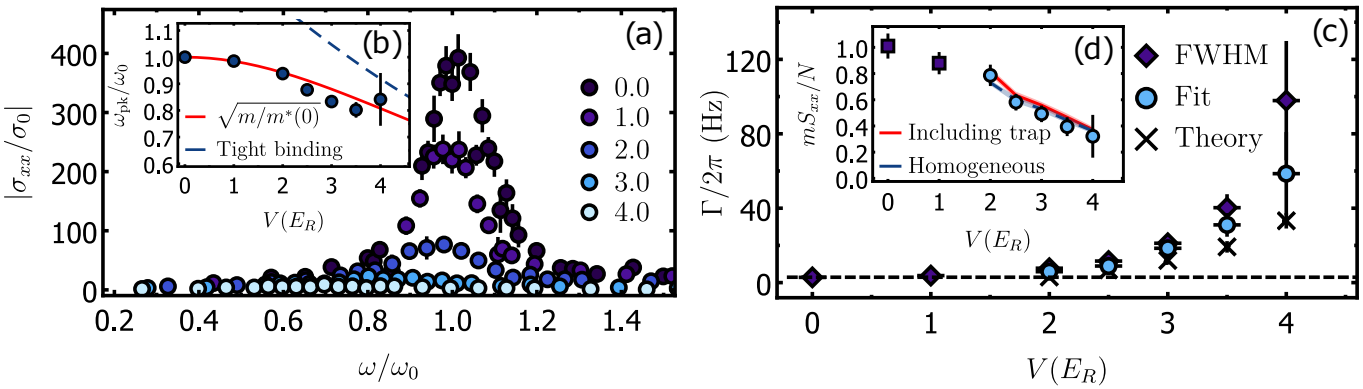

FIG. 7. **Breaking of local translational invariance.** (a) The magnitude of conductivity $|\sigma_{xx}|$ is shown for lattice depths $V/E_R = 0.0$, 1.0, 2.0, 3.0, and 4.0. Peak conductivity falls from $\sim 400\sigma_0$ at $0\,E_R$ to $\sim 15\sigma_0$ at $4\,E_R$. Frequency has been normalized by the bare trap frequency, which changes with lattice beam power. (b) The peak frequency $\omega_{\rm pk}$ is shown versus depth s_L, and compared to the tight-binding approximate $\sqrt{m/m^*}$ (dashed blue line) and the exact $\sqrt{m/m^*}$ (solid red line) at the bottom of the band. (c) The full width at half maximum for the real conductivity is shown (diamond points) versus lattice depth, as determined from a Lorentzian fit. This is compared to the Γ (circles) obtained via the fit procedure described in the text, which isolates for interaction-induced broadening, at depths $s_L \geq 2.0$. The results of kinetic theory are also shown ($\times$). (d) The f-sum S_{xx} (squares show numerically integrated values, circles show fit values) is compared to a Maxwell-Boltzmann prediction for a single-band lattice (dashed blue line) and for a model that includes the harmonic confinement (red solid line), as described in the text.

lattice axes [see Fig.6(e)]. We find that the components of the conductivity tensors obtained through two different choices of pairs of measurement axes possess similar conductivities when recast into a common basis (x', y' as shown).

At each frequency, one can decompose $\sigma_{\alpha\beta}$ into its symmetric and anti-symmetric parts, $\sigma_{\alpha\beta} = \sigma^{(\rm S)}_{\alpha\beta} + \sigma^{(\rm A)}_{\alpha\beta}$. The symmetric conductivity is decomposed into the sum of its real and imaginary parts which are fully characterized by their eigenvalues and the rotation angle for which they are diagonal. In this case, due to the near isotropy of the system, eigenvalues are nearly degenerate and such a rotation-angle is ill-defined. The anti-symmetric $\sigma^{(\rm A)}_{\alpha\beta}$ has only one scalar degree of freedom (in two dimensions), which is the Hall conductivity,

$$\sigma_H = \frac{\sigma_{\alpha\beta} - \sigma_{\beta\alpha}}{2}. \tag{4}$$

and which is invariant under rotation. In Fig. 6(f), we allow for the possibility that an anti-symmetric part of the conductivity tensor exists, and plot its determined value within the frequency band of interest. As expected for our system, σ_H is consistent with zero: there is no broken time-reversal symmetry in the Hamiltonian. This can be further quantified using a sum rule for the off-diagonal conductivity. Defining the Hall angle as $\tan\theta_H = \sigma_H/\sigma_{xx}$ [25] , then

$$\frac{2}{\pi}\int_0^\infty d\omega\, \mathrm{Re}\tan\theta_H = \omega_H \tag{5}$$

where ω_H is the Hall frequency, unaffected by interactions, and is the cyclotron frequency eB/m for a free electron. From our data we find $\omega_H = 2\pi \times (0 \pm 1)\,\mathrm{Hz}$, consistent with zero. Despite the null result of this measurement, it provides a tool to explore Hall physics, and an alternative to the method demonstrated in [26].

Effect of lattice depth on conductivity

A theorem by Kohn [27] is that the center-of-mass response of any harmonically trapped system will be independent of interactions between particles. This fact is regularly exploited in an ultracold atoms experiment, where periodic modulation of a trap is used to calibrate the trap frequency, without a systematic, interaction-induced shift. In this work and in prior studies of c.m. motion in an optical lattice, the same observable acquires new significance due to the breaking of translational invariance by the lattice [21, 28, 29]. Figure 7 demonstrates this effect. At zero lattice depth, the response is a Fourier-limited peak, at the bare trap frequency. As the lattice depth is increased, the Kohn response melts, which manifests in three transformations: a shift in the peak response, a loss of spectral weight, and a broadening.

The frequency shift in peak conductivity is primarily due to the increase in effective mass at the bottom of the band, where the one-dimensional density of states is peaked. For a uniform lattice, the effective mass is given by

$$\frac{1}{m^*_{\alpha\beta}(\vec{k})} \equiv \frac{1}{\hbar^2}\frac{\partial^2\epsilon(\vec{k})}{\partial k_\alpha \partial k_\beta} \tag{6}$$

where $\vec{k}$ is quasi-momentum, $\epsilon(\vec{k}) = \langle\vec{k}|\hat{H}_0|\vec{k}\rangle$, and $\hat{H}_0$ is the kinetic energy Hamiltonian. In the tight-binding limit of a deep lattice, the dispersion relation is sinusoidal, and $m^*(k=0) = \hbar^2/(2t_0 a_L^2)$; at shallower lattice depths, next-nearest-neighbor tunneling terms contribute. We measure the frequency at which the peak in real conductivity occurs, $\omega_{\rm pk}$. As the effective mass of the particles increases, we would expect this peak to shift to $\omega^* \equiv \omega_0\sqrt{m/m^*(0)}$. In Fig. 7(b), the tight-binding $\sqrt{m/m^*(0)}$ and the exact $\sqrt{m/m^*(0)}$ are compared to the measured $\omega_{\rm pk}/\omega_0$. We find excellent agreement with the beyond-tight-binding effective mass.

The loss of spectral weight is quantified by the integrated real conductivity across the observed frequency range. This is an "f-sum", and the subject of several exact sum rules. For global conductivity, one can show that

$$S^\infty_{\alpha\beta} \equiv \frac{1}{\pi}\int_{-\infty}^{\infty} d\omega\, \mathrm{Re}\,\sigma_{\alpha\beta}(\omega) = \frac{N}{i\hbar}\left\langle\left[\hat{R}_\alpha, \hat{J}_\beta\right]\right\rangle \tag{7}$$

where the angle brackets denote a thermal average. The Hamiltonian of the system enters through $\hat{J}_\beta = iN/\hbar[\hat{H}, \hat{R}_\beta]$. Because $\hat{R}_\beta$ is a local operator, its form is unchanged by interactions or by the presence of a trap.

For any complete physical model,

$$S^\infty_{\alpha\beta} = \frac{N}{m}\delta_{\alpha,\beta} \tag{8}$$

independent of temperature, interaction strength, or trapping environment [21].

An experimentally determined $S_{\alpha\beta}$ may differ from the theoretical $S^\infty_{\alpha\beta}$ due to truncation of the measured f-sum at a finite frequency. Figure 7(d) shows that mS_{xx}/N is unity in the absence of a lattice, but is reduced with increasing depth. In our studies, we probe only dynamical response due to low-energy excitations ($\lesssim 200\,$Hz) within the lowest band, and do not probe the (typically kHz) inter-band transitions [30, 31]. A Hubbard model (HM) naturally captures this low-energy response. The on-diagonal response for an isotropic single-band HM gives

$$S_{xx} = -\frac{a_L^2}{\hbar^2}\langle\hat{H}_{0x}\rangle = -\sigma_0\frac{\langle\hat{H}_{0x}\rangle}{\hbar} \tag{9}$$

where $\hat{H}_{0x} = -t_0\sum_i \hat{c}_i^\dagger\hat{c}_{i+1} + \text{h.c.}$ and $\hat{c}_i$ is the anihilation operator for site i. In this case, the f-sum relates to the kinetic energy through $E_K = \sum_\alpha\langle\hat{H}_{0\alpha}\rangle$. An alternate interpretation is to relate the f-sum to a mass, as

$$S_{xx} = N\langle 1/m^*\rangle\,, \tag{10}$$

where $\langle 1/m^*\rangle$ is thermally averaged effective mass. For a completely filled Hubbard band, $\langle 1/m^*(k)\rangle = 0$, $E_K = 0$, $S_{xx} = 0$, and conductivity must be zero. In the Maxwell-Boltzmann limit, $S_{xx} = NI_1(2\beta t_0)/m^*(0)I_0(2\beta t_0)$, where β is the inverse temperature, and $I_n(z)$ is a modified Bessel function. After extending this to include next-nearest and next-next-nearest neighbour hopping, application of the single-band HM expectation to our measured S_{xx} is shown as a blue line in Fig. 7(d), using the temperatures measured at each depth. The agreement is excellent, even though the parabolic confinement is neglected. This is due to the separation of the trap potential and kinetic energy degrees of freedom in the semiclassical limit.

However, including the parabolic confinement potential is essential to understanding the detailed frequency response, including the prominent resonant observed. The simplest extension of the Bloch hamiltonian $\hat{H}_0$ considers the response along a single axis, with $\hat{H}_{\rm LP} = \hat{H}_{0x} + \hat{V}_{{\rm HO},x}$, where $\hat{V}_{{\rm HO},x} = \sum_i \frac{1}{2}m\omega^2 a_L^2 i^2\hat{c}_i^\dagger\hat{c}_i$. The energy spectrum E_p of the non-interacting eigenstates $|\psi_p\rangle$ is well understood [32–34]. There are two regimes: delocalized states at $-2t_0 < E_p \lesssim 2t_0$, and localized states at $E_p \gtrsim 2t_0$. The lowest-energy states are equally separated in energy, and smoothly transform into Bloch states when the trap frequency is reduced. The localized states have an energy that is asymptotically quadratic in p, as their kinetic energy vanishes and they become purely localized states in the potential. They become relevant when temperature is not small compared to $4t_0$. When using this model at low lattice depths, we include the first-order shift of next-nearest and next-next-nearest neighbour hopping terms to the eigenenergies. This ensures that the energetic splitting between the delocalized states has the correct $\hbar\omega^*$ in the weak lattice limit, instead of the tight-binding $\hbar\omega^*$, as shown to be significant in Fig. 7(b).

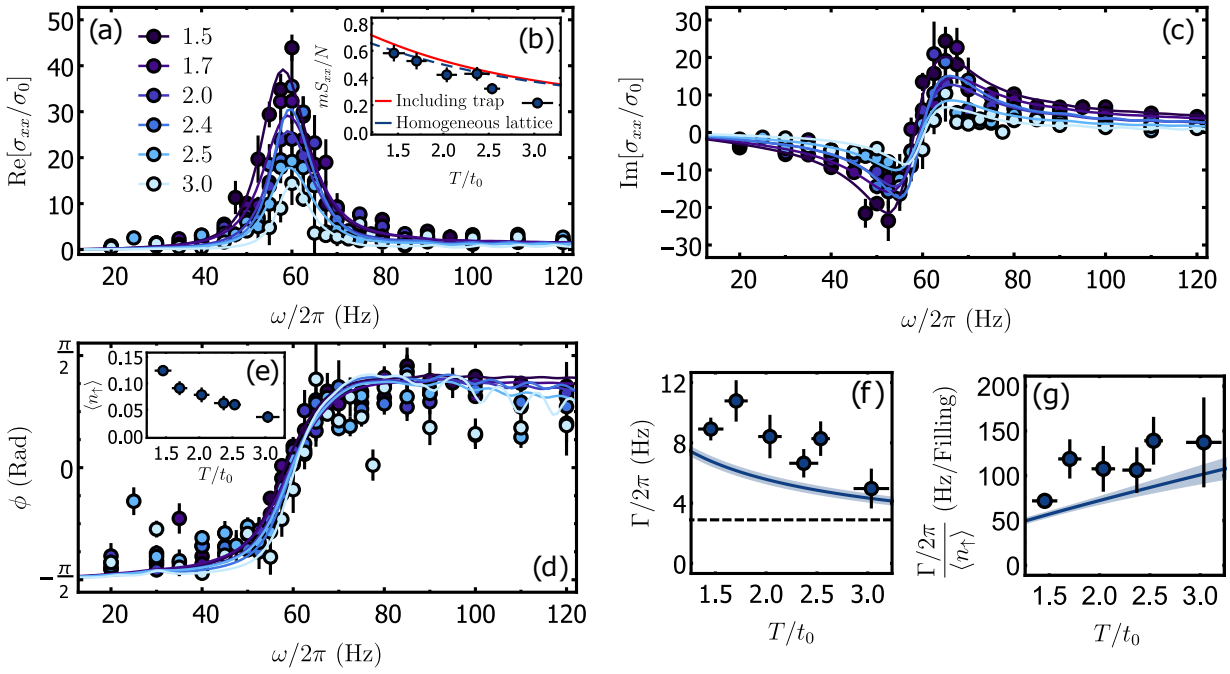

FIG. 8. **Effect of Temperature.** For $s_L = 2.5$ and $U/t_0 = 0.7$, the on-axis conductivity (a) $\mathrm{Re}\,\sigma_{xx}$ was determined for varying temperature. Solid lines show fits to the data using the uniaxial model. The inset (b) shows the f-sum S_{xx} measured from integration of the fit curves in (a) (solid points) as compared to the values theoretically predicted for a homogeneous lattice (dashed blue line) and the uniaxial model (solid red line) using directly measured temperatures. (c) $\mathrm{Im}\,\sigma_{xx}$, and the phase lag of response (d) ϕ, are shown versus temperature T/t_0 from 1.5 to 3.0, as indicated in legend. The phase profile does not change much with increasing temperature, but (e) shows that the measured density per spin state decreases significantly. The fit Γ are shown in (f), and decrease slightly with increasing temperature, but remain above the Fourier-limited value, indicated by the dashed black line. When rescaled by the decreasing density, as shown in (g), it can be seen that scattering rate per particle is increasing with temperature, as expected. Solid blue lines in (f) and (g) indicate the predictions of kinetic theory for indicated temperatures and a fit to the densities.

Treating the drive as a time-dependent perturbation, one can show that the ac conductivity of the LP hamiltonian is

$$\sigma_{xx}^{(\mathrm{LP})}(\omega) = \frac{N\omega}{i\hbar} \sum_{p' \neq p} (f_p - f_{p'}) \frac{|\langle \psi_{p'} | \hat{R}_x | \psi_p \rangle|^2}{\omega - \omega_{pp'} + i\varepsilon} \tag{11}$$

where f_p is the thermal occupation of eigenstate $|p\rangle$, and $\hbar\omega_{pp'} = E_p - E_{p'}$. For the parameters of our experiment, the dominant coupling is between adjacent states, and the frequency spectrum of $\sigma_{xx}^{(\mathrm{LP})}(\omega)$ reflects the energetic spacing between adjacent eigenstates. ε characterizes the $e^{\varepsilon t}$ envelope assumed to describe the adiabatic ramp-up of the excitation potentials. A generalization includes a self-energy term to the denominator of Eq. (11) [35], which in its simplest form replaces ε by a phenomenological broadening $\Gamma/2$, the imaginary part of the self-energy at the frequency of the peak response. Note that $\sigma_{xx}^{(\mathrm{LP})}(\omega)$ obeys Kramers-Kronig relations for any $\Gamma > 0$, and that its f-sum is independent of Γ.

Fitting with the LP model enables a phenomenological broadening Γ to be distinguished from the anharmonicity of the single-particle eigenspectrum. The best-fit Γ, along with numerical FWHM, are shown in Fig. 7(c) versus lattice depth. For $s_L \lesssim 2$, the width is consistent with an independently measured Fourier limit at $\Gamma = 2\pi \times 2.9(2)$ Hz (dashed line), determined by the finite drive time. However at larger s_L, the width is increased due to collisions, as confirmed by agreement with a kinetic theory calculation. This is the clearest sign of the melting of the Kohn response, as the c.m. mode is coupled to other degrees of freedom, and is eventually over-damped by collisions.

Effect of temperature on conductivity

Conductivity is not purely a dynamical response, but includes an essential role of thermodynamics. This is seen through the partial f-sum, as discussed above, which constrains the low-frequency real conductivity. To explore

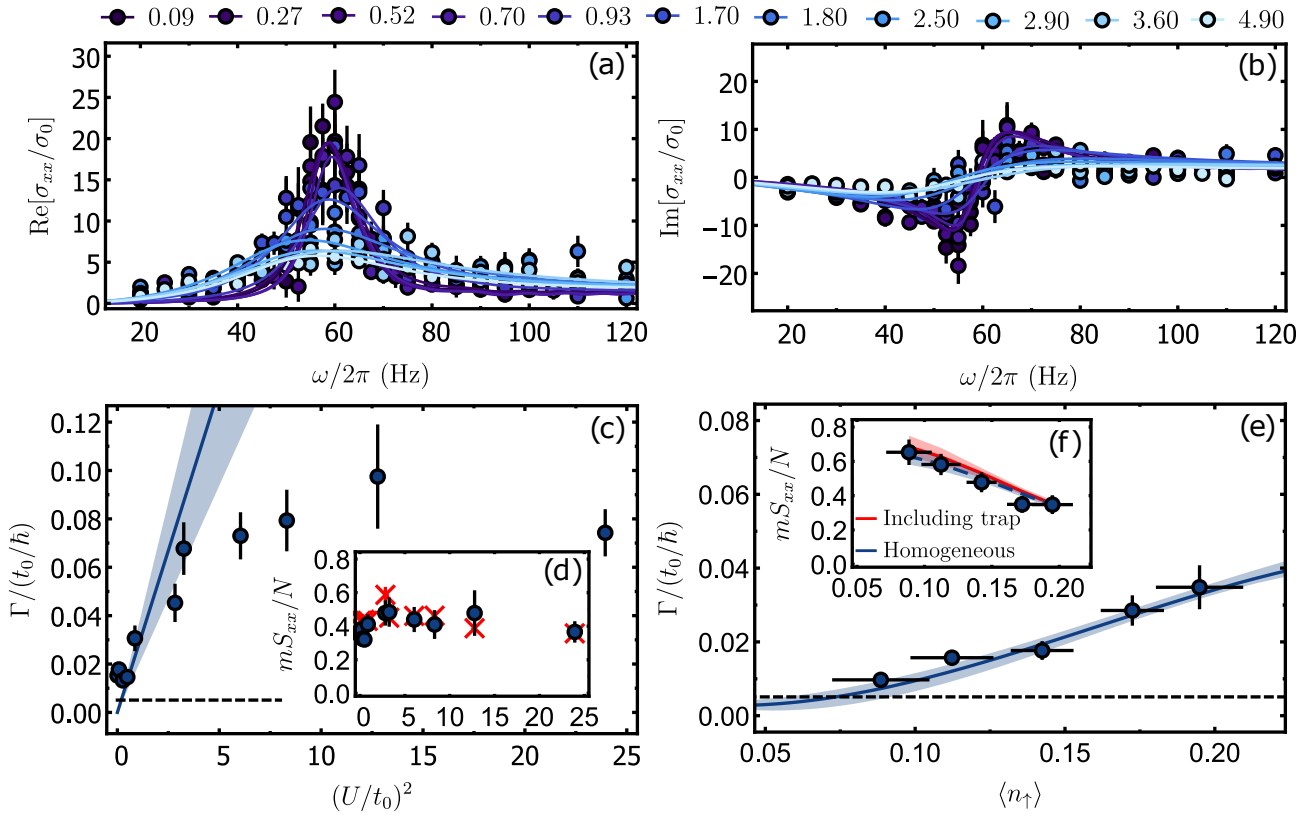

FIG. 9. **Effect of interactions.** Scanning the magnetic field from 20 G to 210 G, the scattering length is tuned via the s-wave Feshbach resonance at 202.1G. The on-axis conductivity (a) $\mathrm{Re}\,\sigma_{xx}$ and (b) $\mathrm{Im}\,\sigma_{xx}$ are shown for $|U/t_0|$ as indicated in the legend. Also shown (lines) are the LP $\sigma_{xx}^{(\mathrm{LP})}$ with best-fit Γ shown in (c) and f-sum S_{xx} shown in (d). The red markers in (d) show the prediction of the LP model using measured temperatures. The same quantities are plotted in (e,f), but with respect to the measured density per spin state, $\langle n_\uparrow \rangle$, with constant $U/t_0 = 0.70$. Blue solid lines in (c) and (e) show the scattering rate calculated in a kinetic theory, and black dashed lines indicate the Fourier-broadened value. All data are for $s_L = 2.5$.

independently the effect of temperature, we measure optical conductivity at variable T, while keeping both lattice depth and scattering length fixed. The temperature is adjusted in the dipole-trap stage of the experimental cycle, by snapping on and off the lattice to a variable height non-adiabatically (in less than 100 μs), then allowing the system to equilibrate, before finally loading to $s_L = 2.5$. Temperature after loading is assessed using in-situ density images.

Each data set of $\mathrm{Re}[\sigma_{xx}]$ and $\mathrm{Im}[\sigma_{xx}]$ is fit to the LP model, using a Maxwell-Boltzmann distribution, measured trap parameters, numerically calculated coupling matrix elements, the beyond-tight-binding eigenfrequencies, and two fit parameters: temperature T and eigenstate width Γ. As seen in Fig. 8, the fits are excellent. From the fits, an analytically-computed f-sum may be extracted.

The primary effect of temperature in this parameter regime is an overall reduction in response: the peak conductivity in Figure 8(a) decreases dramatically with increasing temperature. The decrease in spectral weight is quantified in Figure 8(b), where the S_{xx} is seen to decrease by roughly a factor three as T is doubled. Data are compared to both the f-sum of Eq. 11 at the measured T (instead of best-fit T), and to the uniform-lattice prediction, with good agreement to both. The reduction in f-sum is larger than anticipated in these single-band models at large T, perhaps because of thermal occupation of the next band. However, using a single-band tight-binding interpretation of the f-sum (see Eq. 9), we find a striking signature of the *reduction* of kinetic energy of a lattice gas with temperature, unlike free or harmonically trapped fermions.

Figure 8(f) shows that the best-fit Γ changes only slightly with increasing temperature, and is not far above the Fourier limit. This behaviour is reflected in how the phase profile [Fig. 8(d)] also remains relatively unchanged. The slight decrease in Γ versus temperature is primarily due to a significant decrease in density as temperature increases, as would be expected for a harmonically-trapped system. The average filling per spin-state decreases from $\langle n_\uparrow \rangle = 0.12(1)$ to 0.04(1) from our lowest to highest measured T, as illustrated in Figure 8(e). This reduction in density intuitively reduces the collision rate between particles, which reduces the current-damping rate, and thus the broadening of the response. To correct for this effect, we can instead plot the broadening per unit filling $\Gamma/\langle n_\uparrow \rangle$ in Figure 8(g).

This quantity increases with temperature, in agreement with the expectation that the resistivity of a metal should increase with temperature at constant electron density. Indeed, despite the proximity to the Fourier limit contributing systematic error to the determination of the broadening, data points in Figs. 8(f)(g) remain close to expectations of the kinetic theory calculation (blue lines) discussed below.

Effect of collisions on conductivity

Perhaps the most interesting information one gains from conductivity is the effect of scattering processes on transport. We explore this dependence in two ways: by tuning the scattering length via a Feshbach resonance, and by changing the density by varying the number of atoms loaded into the lattice.

Figure 9 summarizes the effect of these variables on optical conductivity, with data is fit to the LP model. As Γ becomes much larger than the Fourier broadening, it acquires a new significance: $\Gamma \to \tau^{-1}$, the inverse of the transport time. This is a measure of the $1/e$ damping time of particle currents, due to collisions. Since this broadening is fit on top of a theory that already includes the anharmonicity of the single-particle eigenspectrum, we can distinguish scattering from single-particle structure.

The solid lines in Figs. 9(a,b) show fits to the LP model, with resultant Γ and S_{xx} shown in Figs. 9(c,d). The peak conductivity is reduced, however, we find that S_{xx} is nearly constant, with residual small variations [as shown in Fig. 9(d)]. Even these small variations are explained within the *non-interacting* model using the measured T at each U (see red $\times$ symbols). This comparison illustrates a basic property of optical conductivity: scattering cannot "destroy" conductivity, but only move it from one part of the $\mathrm{Re}\,\sigma(\omega)$ spectrum to another [36]. One sees this through the f-sum rules, which depend explicitly on $\langle \hat{H}_0 \rangle$, so that interactions affect the sum rule only through changes in thermodynamics, but not through dynamical and dissipative effects such as scattering.

Instead, scattering reduces the peak conductivity through spectral broadening of the response, shown by an increasing Γ. For $U/t_0 < 2$, we find Γ increases with U^2, as shown in Figs. 9(c) and discussed further below. At larger U, the best-fit Γ deviates from linear, and appears to saturate at $280(80)\,\mathrm{s}^{-1}$, which is $0.08(2)\hbar/t_0$. For these parameters, the effective oscillator is still under-damped: $\Gamma/\omega_0 \sim 0.7(2)$.

The collision rate can alternatively be increased with higher density, which provides an independent measure of the effect of inter-particle interactions on the conductivity spectrum. Figures 9(e,f) show fit results from data sets with $U/t_0 = 0.7$, but measured density changing from 0.09(2) to 0.19(1) per spin state, as controlled by varying the total number of atoms loaded into the lattice from $N = 5 \times 10^3$ to $N = 5 \times 10^4$. We again see that Γ increases well above the Fourier limit, but due to a systematic increase in temperature, S_{xx} is also reduced.

To understand $1/\tau$ in the $U \lesssim t_0$ regime, we calculate the rate of current damping using a kinetic approach. The global current is $\boldsymbol{J} = \boldsymbol{J}_\uparrow + \boldsymbol{J}_\downarrow$, with $\boldsymbol{J}_\uparrow = \sum_{\boldsymbol{q}} f_\uparrow(\boldsymbol{q}) \boldsymbol{v}(\boldsymbol{q})$, where $\boldsymbol{q} = a_L \boldsymbol{k}$ is dimensionless quasimomentum, $f_\uparrow(\boldsymbol{q})$ is the non-equilibrium occupation of eigenstate $|\boldsymbol{q}\rangle$, $v_\alpha(\boldsymbol{q}) = (2t_0 a_L/\hbar)\sin q_\alpha$ in tight binding. The rate of change of current due to collisions is

$$\left.\frac{d}{dt}\right|_{\mathrm{irrev}} \boldsymbol{J}_\uparrow = \sum_{\boldsymbol{q}} \boldsymbol{v}(\boldsymbol{q}) \frac{df_\uparrow(\boldsymbol{q})}{dt} \,. \tag{12}$$

We consider a distribution displaced by Δq_x from an equilibrium Fermi distribution $f^{(\mathrm{eq})}(\boldsymbol{q})$ due to an external force, where $\Delta q_x \ll 1$ in linear response. The rate of relaxation of $f(\boldsymbol{q})$ back to equilibrium may be calculated by treating the Hubbard U as a perturbation that scatters incoming $\boldsymbol{q}_1, \boldsymbol{q}_2$ into final states $\boldsymbol{q}_3$ and $\boldsymbol{q}_4$. The value of $\boldsymbol{q}_4$ is uniquely determined by the other three momenta. When $q_{\alpha,4} = q_{\alpha,1} + q_{\alpha,2} - q_{\alpha,3} \pm 2\pi$ along any lattice axis α, the scattering is called an "Umklapp" collision, in contrast to collisions that conserve quasi-momentum. The amplitude of all types of events is equal in the tight-binding limit.

Retaining only terms that are first order in Δq_x, the ratio of current damping rate to the current is

$$\frac{1}{\tau} = \frac{U^2}{\hbar} \frac{2\pi\beta}{n_\uparrow \langle 1/m^* \rangle} \int \frac{d^3\boldsymbol{q}_1}{2\pi^3} \frac{d^3\boldsymbol{q}_2}{2\pi^3} \frac{d^3\boldsymbol{q}_3}{2\pi^3}\, v_x(\boldsymbol{q}_1)\, \Delta J_x(12;34) f_1^{(\mathrm{eq})} f_2^{(\mathrm{eq})} (1 - f_3^{(\mathrm{eq})})(1 - f_4^{(\mathrm{eq})})\, \delta(E_{34} - E_{12}) \,, \tag{13}$$

where $\Delta J_x(12;34)$ is the change in current along x between the initial and final states, and $f_{1,3}^{(\mathrm{eq})} = f_\uparrow^{(\mathrm{eq})}(\boldsymbol{q}_{1,3})$, and $f_{2,4}^{(\mathrm{eq})} = f_\downarrow^{(\mathrm{eq})}(\boldsymbol{q}_{2,4})$, and the integration is over the Brillouin zone.

The results of the calculation are shown as blue lines in Figures 9(c,e). As interaction strength is varied, the theory predicts a linear scaling in U^2 for the scattering rate. This relation does not deviate far from the measured data for small U/t_0, but cannot account for the saturation of measured scattering rates for larger values, beyond the perturbative regime. For the varying-density data taken at background scattering length, the theory and experiment exhibit excellent agreement within error. The scattering rates appear to scale approximately linearly with increasing

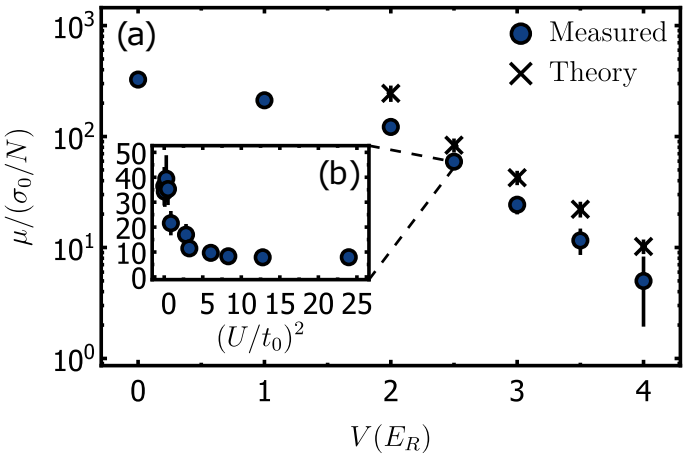

FIG. 10. **Carrier mobility.** (a) Increasing the lattice depth from $0E_R$ to $4E_R$ results in a drastic decrease in the mobility of charge carriers in our system. (b) The inset shows how the mobility at $2.5E_R$ is affected by the varying interaction strengths corresponding to points in Figure 9.

density in the temperature regime explored here, which corresponds to the expected result for a Maxwell-Boltzmann distribution of state occupancy.

We note that τ differs from the mean free time between collisions, since collisions do not necessarily damp current. Kohn's theorem is one dramatic example of this distinction. On the other hand, relaxation of a perturbative displacement in quasimomentum occurs only through collisions that also relax current change the distribution function, which indicates a microscopic similarity between our measurement in a recent study of quasi-momentum relaxation [37].

Mobility

In linear response, an applied impulse $F_x\Delta t$ generates a displacement Δq_x of $f(\boldsymbol{q})$ from equilibrium. It can be shown that the resulting global current per particle is $\Delta J_x/N = F_x\langle 1/m^*\rangle\Delta t$. If the applied force is instead held fixed, the displacement Δq_x will reach a steady state due to current damping. Therefore, in the absence of a trap, the relationship between applied dc force and rate of change of global current is

$$\frac{dJ_{\uparrow x}}{dt} = F_x\left\langle\frac{N_\uparrow}{m^*}\right\rangle - \frac{1}{\tau}J_{\uparrow x}\,. \tag{14}$$

In steady state, $dJ_{\uparrow x}/dt = 0$, and so the drift current per particle is $J_{\rm D}/N = \langle\tau/m^*\rangle F_x$. Apart from a factor of elementary charge, we can identify

$$\mu = \langle\tau/m^*\rangle \tag{15}$$

as the mobility: the ratio between the carrier drift velocity and applied dc force. Since the partial f-sum is $S_{xx} = N\langle 1/m^*\rangle$, mobility combines two main quantities derived from σ_{xx} spectra. Even though both τ and S_{xx} are measured in a trapped system, neither is sensitive to the presence of a trap — comparing well with theoretical models for a uniform lattice system at the same T/t_0 and $\langle n_\uparrow\rangle$. Thus μ as defined here is a measure of the mobility of fermions in a uniform lattice.

Figure 10 shows the dimensionless mobility versus lattice beam power and versus scattering length, combining data previously presented in Figs. 7 and 9. Figure 10(a) shows a dramatic reduction of μ by two orders of magnitude, as s_L increases. This reflects a combination of increasing effective mass m^*, increasing interaction strength U, and increasing density $\langle n_\uparrow\rangle$ due to the increased harmonic confinement, as the lattice depth is increased. As a consequence of the Kohn theorem, one would expect $\mu\to\infty$ as lattice depth is reduced. Here, the observed μ saturates to a finite value due to Fourier-limited spectral precision.

Figure 10(b) demonstrates the decrease in mobility as the scattering length increases, for fixed $s_L = 2.5$. The mobility decreases rapidly in the $U \lesssim t_0$ weakly interacting regime, and then saturates to a steady-state value in the strongly interacting regime, both reflecting the trend in τ^{-1}.

For under-damped current response, the mobility is approximately equal to the peak on-axis real conductivity $\mathrm{Re}\,\sigma_{xx}(\omega)$. One can compare Fig. 10 visually to the peak values of spectra in Figs. 7a and 9a. This correspondence is

precise in the limit where $\mathrm{Re}\,\sigma_{xx}(\omega)$ is Lorentzian: then its peak value $\to S_{xx}\tau = \mu$, so long as $\Gamma = \tau^{-1}$ is not Fourier limited. Peak conductivity in a Drude model, where $\sigma_e(\omega) \sim (1 + i\omega\tau)^{-1}$, is the dc conductivity $\sigma_e(0) = S_e\tau$, where S_e is the low-frequency f-sum. The supports the association of μ with the dc conductivity of an extensive material, in which the trap is removed but average intensive parameters are kept constant. This identification follows the order of limits in which the dc conductivity is defined: first the excitation wavelength $L \to 0$, and then $\omega \to 0$ [36]. However, for a finite-L sample, the same physics corresponds to a finite ω. For our harmonically trapped system, the spacing between the lowest-energy single-particle eigenmodes is $\hbar\omega^*$, so that the lowest-energy eigenstates are probed at finite frequency, where σ_{pk} is found for weak interactions.

III. CUMULATIVE LIST OF PEOPLE INVOLVED IN THE RESEARCH EFFORT IN 2013 – 2018

J. H. Thywissen (PI), Alan Stummer (technician), Stefan Trotzky (Postdoc), Fudong Wang (postdoc), Graham Edge (Ph.D. student), Dylan Jervis (Ph.D. student), Rhys Anderson (Ph.D. student), Vijin Venu(M.Sc. and Ph.D. student), Peihang Xu (Ph.D. student), Ryan Day (M.Sc. student), Geyue Cai (undergraduate visitor from HKUST), Will Cairncross (undergraduate), Fabian Bttcher (graduate visitor from Stuttgart), Tristan Gautie (undergraduate visitor from Ecole Polytechnique), Christian Veit (graduate visitor from Stuttgart).

IV. STUDENT THESES

Dylan Jervis, "A Fermi gas microscope apparatus" (Ph.D. thesis, 2014)

Ryan Day, "Grey Sub-Doppler Cooling of 40K in an Optical Lattice" (M.Sc. thesis, 2014)

Daniel Nino, "Towards Raman Sideband Cooling of 40K Using the 4S1/2 ? 5P1/2 Transition" (M.Sc. thesis, 2015)

Vijin Venu, "Raman cooling in a deep far-detuned optical lattice" (M.Sc. thesis, 2016)

Graham Edge, "Imaging Fermionic Atoms in a Quantum Gas Microscope" (Ph.D. thesis, 2017)

V. PROJECT CHRONOLOGY & MILESTONES

2013.02.01 - Project start 2013.03 - Atoms loaded into three-dimensional optical lattice
2013.07 - Grey molasses cooling in free space
2014.02 - EIT cooling in lattice
2014.04 - Magnetic field stabilization to sub-10-milligaus
2014.07 - Successful D1 laser cooling in lattice
2014.07 - First 405nm fluorescence images: signal weak
2014.08 - Single-plane selection
2014.10- First 770nm fluorescence images: 350x improvement in brightness
2014.11 - Boost lattice power to 900 E_R
2015.03.08 - First single-atom images
2015.07 - Studies of single-atom image fidelity
2015.08 - Brightness and resolution boost with 0.8 NA objective
2016.05 - Successful Raman sideband cooling and imaging
2016.09 - Combined Raman + EIT cooling and imaging
2017.01 - First conductivity measurements
2017.02 - Measure off-diagonal conductivity
2017.03 - Collaboration started with ENS Paris
2017.05 - QMC calculations for in situ thermometry
2017.06 - See melting of Kohn response
2017.Fall - Study effect of interactions, filling
2018.12 - Preprint of optical conductivity work posted on arXiv
2018.01.31 - Project end

[1] G. J. A. Edge, R. Anderson, D. Jervis, D. C. McKay, R. Day, S. Trotzky, and J. H. Thywissen, Phys. Rev. A **92**, 063406 (2015).
[2] E. Haller, J. Hudson, A. Kelly, D. A. Cotta, B. Peaudecerf, G. D. Bruce, and S. Kuhr, Nature Phys. **11**, 738 (2015).
[3] L. W. Cheuk, M. A. Nichols, M. Okan, T. Gersdorf, V. V. Ramasesh, W. S. Bakr, T. Lompe, and M. W. Zwierlein, Phys. Rev. Lett. **114**, 193001 (2015).
[4] M. F. Parsons, F. Huber, A. Mazurenko, C. S. Chiu, W. Setiawan, K. Wooley-Brown, S. Blatt, and M. Greiner, Phys. Rev. Lett. **114**, 213002 (2015).
[5] A. Omran, M. Boll, T. A. Hilker, K. Kleinlein, G. Salomon, I. Bloch, and C. Gross, Phys. Rev. Lett. **115**, 263001 (2015).
[6] M. Miranda, R. Inoue, Y. Okuyama, A. Nakamoto, and M. Kozuma, Phys. Rev. A **91**, 063414 (2015).
[7] K. D. Nelson, X. Li, and D. S. Weiss, Nature Phys. **3**, 556 (2007).
[8] W. S. Bakr, J. I. Gillen, A. Peng, S. Foelling, and M. Greiner, Nature **462**, 74 (2009).
[9] J. F. Sherson, C. Weitenberg, M. Endres, M. Cheneau, I. Bloch, and S. Kuhr, Nature **467**, 68 (2010).
[10] D. Rio Fernandes, F. Sievers, N. Kretzschmar, S. Wu, C. Salomon, and F. Chevy, Europhys. Lett. **100**, 63001 (2012).
[11] A. T. Grier, I. Ferrier-Barbut, B. S. Rem, M. Delehaye, L. Khaykovich, F. Chevy, and C. Salomon, Phys. Rev. A **87**, 063411 (2013).
[12] D. Nath, R. K. Easwaran, G. Rajalakshmi, and C. S. Unnikrishnan, Phys. Rev. A **88**, 053407 (2013).
[13] G. Salomon, L. Fouché, P. Wang, A. Aspect, P. Bouyer, and T. Bourdel, Europhys. Lett. **104**, 63002 (2013).
[14] A. Burchianti, G. Valtolina, J. A. Seman, E. Pace, M. DePas, M. Inguscio, M. Zaccanti, and G. Roati, Phys. Rev. A **90**, 043408 (2014).
[15] G. Grynberg and J. Y. Courtois, Europhys. Lett. **27**, 41 (1994); M. Weidemuller, T. Esslinger, M. A. Olshanii, A. Hemmerich, and T. W. Hänsch, Europhys. Lett. **27**, 109 (1994); D. Boiron, C. Triche, D. R. Meacher, P. Verkerk, and G. Grynberg, Phys. Rev. A **52**, R3425 (1995).
[16] G. Morigi, J. Eschner, and C. H. Keitel, Phys. Rev. Lett. **85**, 4458 (2000); G. Morigi, Phys. Rev. A **67**, 033402 (2003); C. F. Roos, D. Leibfried, A. Mundt, F. Schmidt-Kaler, J. Eschner, and R. Blatt, Phys. Rev. Lett. **85**, 5547 (2000); M. Mücke, E. Figueroa, J. Bochmann, C. Hahn, K. Murr, S. Ritter, C. J. Villas-Boas, and G. Rempe, Nature **465**, 755 (2010).
[17] V. Vuletic, C. Chin, A. J. Kerman, and S. Chu, Phys. Rev. Lett. **81**, 5768 (1998).
[18] D. J. Han, S. Wolf, S. Oliver, C. McCormick, M. T. DePue, and D. S. Weiss, Phys. Rev. Lett. **85**, 724 (2000).
[19] Y. S. Patil, S. Chakram, L. M. Aycock, and M. Vengalattore, Phys. Rev. A **90**, 033422 (2014).
[20] R. Anderson, F. Wang, P. Xu, V. Venu, S. Trotzky, F. Chevy, and J. H. Thywissen, "Optical conductivity of a quantum gas," (2017), arXiv:1712.09965.
[21] Z. Wu, E. Taylor, and E. Zaremba, Europhys. Lett. **110**, 26002 (2015).
[22] A. Tokuno and T. Giamarchi, Phys. Rev. Lett. **106**, 205301 (2011).
[23] D. N. Basov and T. Timusk, Rev. Mod. Phys. **77**, 721 (2005).
[24] R. Senaratne, S. V. Rajagopal, T. Shimasaki, P. E. Dotti, K. M. Fujiwara, K. Singh, Z. A. Geiger, and D. M. Weld, arXiv (2017), 1711.02654.
[25] H. D. Drew and P. Coleman, Phys. Rev. Lett. **78**, 1572 (1997).
[26] L. J. LeBlanc, K. Jimenez-Garcia, R. A. Williams, M. C. Beeler, A. R. Perry, W. D. Phillips, and I. B. Spielman, Proc. Nat. Acad. Sci. **109**, 10811 (2012).
[27] W. Kohn, Phys. Rev. **123**, 1242 (1961).
[28] G. Orso, L. P. Pitaevskii, and S. Stringari, Phys. Rev. Lett. **93**, 020404 (2004).
[29] Z. Wu and E. Zaremba, Ann. Phys. **342**, 214 (2014).
[30] J. Heinze, J. S. Krauser, N. Fläschner, B. Hundt, S. Götze, A. P. Itin, L. Mathey, K. Sengstock, and C. Becker, Phys. Rev. Lett. **110**, 085302 (2013).
[31] M. Reitter, J. Näger, K. Wintersperger, C. Sträter, I. Bloch, A. Eckardt, and U. Schneider, Phys. Rev. Lett. **119**, 200402 (2017).
[32] C. Hooley and J. Quintanilla, Phys. Rev. Lett. **93**, 198 (2004).
[33] A. M. Rey, G. Pupillo, C. W. Clark, and C. J. Williams, Phys. Rev. A **72**, 033616 (2005).
[34] H. Ott, E. de Mirandes, F. Ferlaino, G. Roati, V. Türck, G. Modugno, and M. Inguscio, Phys. Rev. Lett. **93**, 120407 (2004).
[35] P. B. Allen, Phys. Rev. B **92**, 054305 (2015).
[36] G. D. Mahan, *Many-Particle Physics*, 3rd ed. (Springer, New York, 2000).
[37] W. Xu, W. McGehee, W. Morong, and B. DeMarco, arXiv (2016), 1606.06669v2.